PCCP

ROYAL SOCIETY OF CHEMISTRY

PAPER

View Article Online
View Journal | View Issue

Cite this: *Phys. Chem. Chem. Phys.*, 2022, **24**, 7014

Elliptic dichroism in strong-field ionization of atoms subjected to tailored laser fields

Wilhelm Becker *[a] and Dejan B. Milošević [abc]

The differential ionization rate for strong-field ionization by tailored laser fields of atomic systems averaged over the magnetic quantum number satisfies particular inversion and reflection symmetries. The symmetries of the elliptic-dichroism parameter, which is related to the change of sign of the ellipticity of the laser field, are considered in detail, with particular emphasis on high-order above-threshold ionization. The general results are illustrated by the examples of an elliptically polarized laser field and a bi-elliptical orthogonally polarized two-color (BEOTC) field. For the BEOTC field the differential ionization rate and the elliptic-dichroism parameter are investigated for the ω–2ω and ω–3ω field combinations and for various relative phases between the laser-field components. The inversion and reflection symmetries of the photoelectron momentum distribution in the polarization plane of the field depend on the parities of r and s in the $r\omega$–$s\omega$ BEOTC field combination and on the relative phase between the field components. We suggest that, by analyzing the symmetry properties of the measured momentum distribution of the elliptic-dichroism parameter, one can identify the mechanism of strong-field ionization. If the rescattering mechanism is dominant one can use these distributions to obtain information about the atomic and molecular structure and dynamics.

Received 13th November 2021,
Accepted 23rd February 2022

DOI: 10.1039/d1cp05209h

rsc.li/pccp

1 Introduction

Dichroic effects provide a versatile tool for modern physics and chemistry.[1] For photoionization, two limiting cases can be identified: photoelectric circular dichroism (PECD) refers to a backward/forward asymmetry of the electron yield in the propagation direction of the incident circularly polarized laser beam, which is observed for a target of nonoriented chiral molecules. In contrast to earlier dichroic effects, this is due to the electric rather than the magnetic dipole. Hence the effect is substantial and has important applications especially for chiral recognition in the gas phase. Alternatively, circular (or elliptical) dichroism in the angular distribution (CDAD) refers to the effect of a change of the polarization state of the incident light on the momentum distribution within the polarization plane of photoelectrons released by a usually nonchiral target: "…, the CDAD effect disappears in directions parallel to the photon beam, whereas PECD asymmetry is maximized in these directions. Conversely, the PECD asymmetry disappears in directions perpendicular to the photon beam where the maximum CDAD asymmetry can be found".[1] CDAD can be used to analyze the interaction of light with a nonchiral target in order to assess the relative weight of nonadiabatic *versus* adiabatic ionization mechanisms. In other words, it allows one to attribute features of the momentum distribution to processes that require or do not require interaction of the freed electron with the parent ion.

The first theoretical formulation of PECD was given in ref. 2 and the first observations were reported in ref. 3 and 4. Dichroic effects were observed in one-photon ionization and subsequently also in multiphoton ionization,[5,6] above-threshold ionization (ATI)[7] and, in general, in strong-field ionization.[8–11] Currently, in addition to the photo-ion circular dichroism (PICD),[12] PECD appears to open up the best avenue towards efficient chiral recognition.[4,13] The term PECD has also been used for backward/forward asymmetries caused by orthogonally polarized two-color (OTC) fields.[14]

Left-right asymmetries in the photoelectron angular distributions of ATI by an elliptically polarized laser field were first reported in ref. 15, which has initiated many subsequent studies.[16–20] In the present paper we consider CDAD, more precisely elliptic dichroism (EDAD) in strong-field ionization and, in particular, in above-threshold ionization (ATI) and high-order above-threshold ionization (HATI).

High-order strong-laser-field-driven processes are usually explained using the three-step model: the electron, temporarily liberated from an atom or molecule (this is the first or ionization step) may be driven back by the field (propagation step) to

[a] *Max-Born-Institut, Max-Born-Strasse 2a, 12489 Berlin, Germany. E-mail: wbecker@mbi-berlin.de*
[b] *University of Sarajevo – Faculty of Science, Zmaja od Bosne 35, 71000 Sarajevo, Bosnia and Herzegovina. E-mail: milo@bih.net.ba*
[c] *Academy of Sciences and Arts of Bosnia and Herzegovina, Bistrik 7, 71000 Sarajevo, Bosnia and Herzegovina*

interact with the parent ion in the third step. If this interaction is elastic backscattering, then in the resulting process (called HATI) the electron can significantly increase its energy. Another possibility is recombination of this electron with the parent ion followed by emission of a high-energy photon (this is the so-called high-order harmonic generation). We also mention nonsequential multiple ionization, the process in which the recolliding electron kicks out one or more electrons of the parent ion. Such three-step processes have been usually examined using linearly polarized fields since the electron, driven by such a field, can readily revisit the parent ion. In the more general case of an elliptically polarized field, the liberated electron, if it starts with zero momentum, will "miss" its parent ion (*i.e.*, in the language of quantum mechanics, the overlap of the corresponding wave packets will be small), so that the probability of the afore-mentioned high-order processes becomes lower and lower with increasing ellipticity.

For linear polarization and elastic rescattering by the angle 180° (backscattering) the final electron energy can be as high as $10U_p$ (U_p is the electron ponderomotive energy in the laser field), which is five times larger than the maximum energy of the directly ionized (ATI) electrons. The electron can rescatter in any direction, including forward scattering. In this case, the corresponding final electron energy is lower ($<2U_p$). Usually, electrons that do not undergo rescattering (called direct electrons) make the main contribution in this energy region. However, Coulomb effects can enhance the contribution of the forward-scattered electrons since the Coulomb scattering cross section is very large for small angles.[21] In fact, the low-energy structures (LES) in the energy region $<0.1U_p$, discovered in 2009[22,23] (see Section 4 in ref. 24), were attributed to forward scattering.[25] In addition to the LES, the forward-scattered electrons in the region (1–2)U_p generate various interesting structures especially off the polarization axis,[26] most of which have been observed. By interference with the direct electrons, they cause the spiderlike structures known as holograms.[27,28] In our quantum-orbit nomenclature, these orbits are denoted as $\nu\mu = 10$.[29,30]

More recently, it has been confirmed that there are more complex field configurations that also allow the electron to return to its parent ion so that high-order processes can occur more easily. Such, so-called tailored, fields consist of two or more field components having different frequencies and polarizations (see, for example, the special issue about dynamics in tailored ultrashort light fields[31]). For example, a bicircular field is a superposition of two coplanar counter-rotating circularly polarized fields having different frequencies. The HATI process in such a field was considered, for example, in ref. 32 where the improved strong-field approximation, which we will use in the present paper, was presented in detail. As another example, the helicity asymmetry of HATI by an intense bicircular field was analyzed in ref. 18. The helicity-asymmetry parameter defined in this reference is a special case of the elliptic-dichroism parameter to be introduced in the present paper. More recently, circular dichroism in biharmonic ionization of atoms was investigated in ref. 20. Another example of a tailored field is the OTC field, which consists of two linearly polarized components with orthogonal polarizations and commensurable frequencies. A detailed list of references devoted to strong-field processes in OTC fields can be found in ref. 33. Bicircular and OTC fields are special cases of a bi-elliptical OTC (BEOTC) field, which was introduced in ref. 34. As far as we know, the HATI process in a BEOTC field has not been investigated yet. This will make up a major part of this paper.

We will focus on the symmetries obeyed by the angle-resolved spectrum or the velocity map of the liberated electron. A parametric plot of the vector potential of the driving field may exhibit two kinds of symmetries, rotational symmetries and inversion symmetry ($\mathbf{r} \rightarrow -\mathbf{r}$) on the one hand and reflection symmetry with respect to one or several planes (*e.g.* $x \rightarrow -x$ or $y \rightarrow -y$) on the other.[18] The first type preserves the direction of the time evolution of the vector potential while the second one reverses it. The overall shape of the velocity map of the released electron is closely related to the symmetries of the vector potential. ATI electrons, which are described by the lowest-order term of a Born expansion of the ionization amplitude in terms of the binding potential, observe both of the afore-mentioned symmetries. In contrast, HATI electrons undergo rescattering. Hence, they are only captured by the next-order term of the Born series, which allows for one additional interaction with the binding potential. This term depends on the time evolution of the field: ionization precedes rescattering. Therefore, the momentum distribution of the HATI electrons only reproduces the first type of symmetries, which does not depend on the direction of the time evolution. A reversal of the helicities of the driving field corresponds to time reversal. Hence, it leaves the first type intact but not the second. This is most clearly brought out by the dichroism parameter to be defined below. Nonzero values of this parameter immediately pinpoint regions where rescattering makes the dominant contributions. The other way around, given a momentum distribution obtained from an experiment or from numerical solution of the time-dependent Schrödinger equation, an analysis of the field symmetries preserved *versus* those violated allows one to conclude whether or not electrons with certain momenta have undergone rescattering.

We will analyze in detail the dependence of the differential ionization rate and the elliptic dichroism parameter on the parameters of the BEOTC field. We will start our scrutiny with the simpler case of just one elliptically polarized field and investigate the effect of the sign of the ellipticity especially on the various low-energy structures. In Subsection 2.1 we briefly sketch the formalism that we will utilize, *viz.* the strong-field approximation for both the direct and the rescattered electrons. In Subsection 2.2 we introduce the fields that we will investigate, discuss their symmetry properties and the ensuing symmetries of the angle-resolved spectrum of the liberated electrons. Section 3 exhibits the results for the two field configurations, Subsection 3.1 for the elliptically polarized field and Subsection 3.2 for the BEOTC field. We compare the results for two wavelengths, 1300 and 2000 nm. The final Section 4 presents conclusions. We use atomic units throughout the paper.

2 Theory

2.1 Differential ionization rate and the improved strong-field approximation

The differential ionization rate for detection of an electron with the momentum $\mathbf{p}$ and with absorption of n photons from the laser field is given by[32,35]

$$\bar{w}_{\mathbf{p}E_i\ell}(n) = \frac{N_e}{2\ell+1}\sum_{m=-\ell}^{\ell} w_{\mathbf{p}E_i\ell m}(n). \quad (1)$$

We supposed that different electrons from the ground-state configuration of an atom with the ionization potential $I_p = -E_i > 0$ can play the role of the active electron in the single-active-electron approximation we are using. The number of equivalent electrons in the ionizing shell of the atom is N_e and we average over all possible values of the magnetic quantum number m. We consider the case of closed subshells specified by the orbital quantum number ℓ (there are $2\ell + 1$ orbitals enumerated by m). Since each orbital can be occupied by two electrons with opposite values of the spin projections we have $N_e = 2(2\ell + 1)$. For the He atom it is $\ell = m = 0$, while for the other inert gases (Ne, Ar, Kr, Xe) we have $\ell = 1$, $m = 0, \pm 1$. We will illustrate our theoretical results using the example of the Ar atom, which has the ionization potential $I_p = 15.76$ eV.

Within the improved strong-field approximation we have[32,35–37]

$$w_{\mathbf{p}E_i\ell m}(n) \approx 2\pi p\left|T^{\mathrm{dir}}_{\mathbf{p}E_i\ell m}(n) + T^{\mathrm{res}}_{\mathbf{p}E_i\ell m}(n)\right|^2, \quad (2)$$

with the energy-conservation condition $n\omega = E_{\mathbf{p}} - E_i + U_p$, where $U_p = \int_0^T \mathrm{d}t\mathbf{A}^2(t)/(2T)$ is the ponderomotive energy, $T = 2\pi/\omega$ the period, and ω the fundamental angular frequency of the laser field. We use the dipole approximation and the length gauge with the electric field vector $\mathbf{E}(t) = -\mathrm{d}\mathbf{A}(t)/\mathrm{d}t$. The so-called direct-ionization T-matrix element is

$$T^{\mathrm{dir}}_{\mathbf{p}E_i\ell m}(n) = \int_0^T \frac{\mathrm{d}t_0}{T}\langle \mathbf{p} + \mathbf{A}(t_0)|\mathbf{r}\cdot\mathbf{E}(t_0)|\psi_{E_i\ell m}\rangle \mathrm{e}^{i[S_{\mathbf{p}}(t_0) - E_i t_0]}. \quad (3)$$

where $\mathrm{d}S_{\mathbf{q}}(t)/\mathrm{d}t = [\mathbf{q} + \mathbf{A}(t)]^2/2$ and $|\mathbf{q}\rangle$ is a plane-wave ket vector such that $\langle \mathbf{r}|\mathbf{q}\rangle = (2\pi)^{-3/2}\exp(i\mathbf{q}\cdot\mathbf{r})$. The integral over the ionization time t_0 during one optical cycle can be calculated numerically or using the saddle-point method. In (3) the term $S_{\mathbf{p}}(t_0) - E_i t_0$ can be replaced with $\mathbf{p}\cdot\boldsymbol{\alpha}(t_0) + \mathscr{U}(t_0) + n\omega t_0$, where $\mathbf{A}(t) = \mathrm{d}\boldsymbol{\alpha}(t)/\mathrm{d}t$ and $\mathrm{d}\mathscr{U}(t)/\mathrm{d}t + U_p = \mathbf{A}^2(t)/2$. In our approach, the ground-state wave functions $\psi_{E_i\ell m}$ are calculated using the Hartree–Fock–Roothan method and presented in the form of a linear combination of Slater-type orbitals.[32,35]

The rescattering T-matrix element $T^{\mathrm{res}}_{\mathbf{p}E_i\ell m}(n)$ describes the so-called three-step process (see the review articles[36,37] and references therein) in which the liberated electron returns to the parent ion and rescatters off it (*i.e.*, off the corresponding potential $V(\mathbf{r})$, which we model by a double Yukawa potential as described in ref. 35 and 38), reaching the detector with the final momentum $\mathbf{p}$. It is given by

$$T^{\mathrm{res}}_{\mathbf{p}E_i\ell m}(n) = -i\int_0^T \frac{\mathrm{d}t}{T}\mathrm{e}^{iS_{\mathbf{p}}(t)}\int_0^\infty \mathrm{d}\tau\left(\frac{2\pi}{i\tau}\right)^{3/2}\langle \mathbf{p}|V(\mathbf{r})|\mathbf{k}_{\mathrm{st}}(t,\tau)\rangle \times \langle \mathbf{k}_{\mathrm{st}}(t,\tau) + \mathbf{A}(t_0)|\mathbf{r}\cdot\mathbf{E}(t_0)|\psi_{E_i\ell m}\rangle \mathrm{e}^{iS_{\mathbf{k}_{\mathrm{st}}E_i}(t,t_0)}, \quad (4)$$

where the integral is over the rescattering time t and the travel time τ (the ionization time is $t_0 = t - \tau$), $\mathbf{k}_{\mathrm{st}}(t,\tau) = -\frac{1}{\tau}\int_{t-\tau}^{t}\mathrm{d}t'\mathbf{A}(t')$ is the stationary electron momentum, $S_{\mathbf{q}E}(t,t_0) \equiv S_{\mathbf{q}}(t_0) - Et_0 - S_{\mathbf{q}}(t)$ and the term $S_{\mathbf{q}}(t) - E_i t_0$ can be replaced by $\mathbf{p}\cdot\boldsymbol{\alpha}(t) + \mathscr{U}(t) + n\omega t + E_i\tau$. As before, the double integral in eqn (4) can be calculated numerically or using the saddle-point method. The matrix elements in eqn (3) and (4) can be calculated analytically. For inert gases with $\ell = 1$ the matrix element for $m = 0$ is equal to zero, so that only the contributions with $m = \pm 1$ have to be taken into account in (1).

2.2 Inversion and reflection symmetries

An elliptically polarized laser field with the frequency $\omega_1 = r\omega$ (r integer), amplitude E_1 and ellipticity ε_1 has the form

$$\mathbf{E}_1(t) = \frac{E_1}{\sqrt{1+\varepsilon_1^2}}\left(\hat{\mathbf{e}}_x \sin\omega_1 t - \hat{\mathbf{e}}_y\varepsilon_1\cos\omega_1 t\right), \quad (5)$$

where the unit polarization vectors $\hat{\mathbf{e}}_x$ and $\hat{\mathbf{e}}_y$ determine the xy polarization plane. The quantization axis of the atom is the z axis and we consider electrons emitted in the polarization plane of the laser field under the angle θ with respect to the x axis, *i.e.*, the photoelectron momentum in polar coordinates in the xy plane is $\mathbf{p} = (p,\theta)$, with $\cos\theta = \hat{\mathbf{p}}\cdot\hat{\mathbf{e}}_x$ and $\tan\theta = p_y/p_x$. To cover the most general case where $p_z \neq 0$, the ionization potential I_p has to be replaced by $I_p + {p_z}^2/2$.

The exact differential ionization rate $w(\mathbf{p},\varepsilon) \equiv w_{\mathbf{p}Ei\ell m}(n)$ for the field (5) (with the notation $\varepsilon = \varepsilon_1$) satisfies the inversion symmetry (twofold symmetry) $w(-\mathbf{p},\varepsilon) = w(\mathbf{p},\varepsilon)$, *i.e.*, $w(\theta) = w(\theta + \pi)$. This can be shown by rewriting the transition amplitude in the interaction representation as[39] $M_{\mathbf{p}E_i\ell m}(\varepsilon) = \langle \mathbf{p}|\hat{T}\exp\left[-i\int_{-\infty}^{\infty}\mathrm{d}tH_I(t)\right]|\psi_{E_i\ell m}\rangle$, with $\hat{T}$ the time ordering operator, $H_I(t) = \mathrm{e}^{iH_0t}\mathbf{r}\cdot\mathbf{E}(t)\mathrm{e}^{-iH_0t}$ and $H_0 = (-i\partial/\partial\mathbf{r})^2/2 + V(\mathbf{r})$. Introducing the parity operator $\hat{P}$ we have $\hat{P}|\mathbf{p}\rangle = |-\mathbf{p}\rangle$ and $\hat{P}|\psi_{Ei\ell m}\rangle = (-1)^{\ell}|\psi_{Ei\ell m}\rangle$, where we used the following relation for the spherical harmonics: $\hat{P}Y_{\ell m}(\vartheta,\varphi) = Y_{\ell m}(\pi - \vartheta,\varphi + \pi) = (-1)^{\ell}Y_{\ell m}(\vartheta,\varphi)$. We get $M_{-\mathbf{p}E_i\ell m}(\varepsilon) = \langle \mathbf{p}|\hat{P}\hat{T}\exp\left[-i\int_{-\infty}^{\infty}\mathrm{d}tH_I(t)\right]\hat{P}\hat{P}|\psi_{E_i\ell m}\rangle$. The parity operator changes the sign of the exponent in the time-ordered exponential. Using the substitution $t \to t + T/2$ and the relation $\mathbf{E}_1(t + T/2) = -\mathbf{E}_1(t)$ we obtain that, up to a phase factor, $M_{-\mathbf{p}Ei\ell m}(\varepsilon)$ is equal to $M_{\mathbf{p}Ei\ell m}(\varepsilon)$ so that the relation $w(-\mathbf{p},\varepsilon) = w(\mathbf{p},\varepsilon)$ is proven for the exact ionization rate.

There are additional exact symmetries related to a change of the sign of the ellipticity, *i.e.*, a change of the handedness.[39] They are valid for the differential ionization rate (1), which is averaged over the magnetic quantum number m. In order to prove these symmetries we introduce the operators $\hat{P}_x$ and $\hat{P}_y$ of the reflections about the x and y axes in the polarization plane

and use the relations $\hat{P}_x Y_{\ell m}(\vartheta,\varphi) = Y_{\ell m}(\vartheta,\pi-\varphi) = Y_{\ell -m}(\vartheta,\varphi)$ and $\hat{P}_y Y_{\ell m}(\vartheta,\varphi) = Y_{\ell m}(\vartheta,-\varphi) = Y_{\ell -m}(\vartheta,\varphi)$. As in the above derivation of the inversion symmetry, it can be proven that, up to a phase factor, $M_{-p_x p_y E_i \ell' -m}(-\varepsilon)$ is equal to $M_{p_x p_y E_i \ell' m}(\varepsilon)$. A similar derivation can be done for the y component. The only difference is that for $p_y \to -p_y$ it is not necessary to perform the time translation $t \to t + T/2$ because a simultaneous application of $\hat{P}_y$ and the operation $\varepsilon \to -\varepsilon$ leaves the field $\mathbf{E}_1(t)$ unchanged. Therefore, denoting $\bar{w}(\mathbf{p},\varepsilon) \equiv \bar{w}_{\mathbf{p}E_i\ell'}(n)$, we have $\bar{w}(-p_x,p_y,-\varepsilon) = \bar{w}(p_x,-p_y,-\varepsilon) = \bar{w}(p_x,p_y,\varepsilon)$, *i.e.*, $\bar{w}(\pi-\theta,-\varepsilon) = \bar{w}(-\theta,-\varepsilon) = \bar{w}(\theta,\varepsilon)$ or

$$\bar{w}(\theta,-\varepsilon) = \bar{w}(\pi-\theta,\varepsilon). \tag{6}$$

For linear polarization ($\varepsilon = 0$) this means $\bar{w}(-\theta) = \bar{w}(\theta)$.

For the direct electrons, we have the fourfold symmetry:[39] $\bar{w}^{\mathrm{dir}}(\theta,\varepsilon) = \bar{w}^{\mathrm{dir}}(\pi-\theta,\varepsilon) = \bar{w}^{\mathrm{dir}}(-\theta,\varepsilon)$, and the symmetry $\bar{w}^{\mathrm{dir}}(\mathbf{p},\varepsilon) = \bar{w}^{\mathrm{dir}}(\mathbf{p},-\varepsilon)$ upon a change of helicity. This symmetry can be proven using time inversion, *i.e.*, the substitution $t \to -t$, which leads to $M_{\mathbf{p}E_i\ell m}(\varepsilon) \to M^*_{\mathbf{p}E_i\ell m}(-\varepsilon)$ so that the rate (1) for the direct electrons is unchanged. This symmetry is not valid for the rescattering amplitude since in this case the time ordering is important (rescattering follows ionization and not *vice versa*). If we define the elliptic-dichroism parameter[40]

$$\delta(\mathbf{p},\varepsilon) \equiv \frac{\bar{w}(\mathbf{p},\varepsilon) - \bar{w}(\mathbf{p},-\varepsilon)}{\bar{w}(\mathbf{p},\varepsilon) + \bar{w}(\mathbf{p},-\varepsilon)}, \tag{7}$$

the relation $\bar{w}^{\mathrm{dir}}(\mathbf{p},\varepsilon) = \bar{w}^{\mathrm{dir}}(\mathbf{p},-\varepsilon)$ has the consequence that $\delta^{\mathrm{dir}}(\mathbf{p},\varepsilon) = 0$. The above-mentioned exact symmetries lead to the relations $\bar{w}(\theta,\varepsilon) = \bar{w}(\theta+\pi,\varepsilon)$ and $\bar{w}(\theta,\varepsilon) - \bar{w}(\theta,-\varepsilon) = \bar{w}(\pi-\theta,-\varepsilon) - \bar{w}(\pi-\theta,\varepsilon)$, so that $\int_0^\pi [\bar{w}(\theta,\varepsilon) - \bar{w}(\theta,-\varepsilon)]\mathrm{d}\theta = 0$. That is, the exact ionization rate integrated over all angles is independent of the sign of the ellipticity. Therefore, to analyze dichroism, the restricted angle interval $\theta \in [0,\pi/2]$ should be used. In this case we define $\bar{W}(E_\mathbf{p},\varepsilon) = \int_0^{\pi/2} \bar{w}(\varepsilon,\theta)\mathrm{d}\theta$ where the integration extends only over one hemisphere and introduce the angle-integrated elliptic-dichroism parameter[40]

$$\Delta(E_\mathbf{p},\varepsilon) \equiv \frac{\bar{W}(E_\mathbf{p},\varepsilon) - \bar{W}(E_\mathbf{p},-\varepsilon)}{\bar{W}(E_\mathbf{p},\varepsilon) + \bar{W}(E_\mathbf{p},-\varepsilon)}. \tag{8}$$

In ref. 34, we considered the so-called BEOTC (bi-elliptical orthogonal two-color) field. It consists of the elliptically polarized field $\mathbf{E}_1(t)$, eqn (5), having the x axis as the major axis and a second coplanar elliptically polarized field $\mathbf{E}_2(t)$ with the y axis as the major axis and with the frequency $\omega_2 = s\omega$ (s integer), amplitude $\mathbf{E}_2$, and ellipticity ε_2:

$$\mathbf{E}_2(t;\phi) = \frac{E_2}{\sqrt{1+\varepsilon_2{}^2}}\left[\hat{\mathbf{e}}_y \sin(\omega_2 t+\phi) - \hat{\mathbf{e}}_x \varepsilon_2 \cos(\omega_2 t+\phi)\right] \tag{9}$$

so that

$$\mathbf{E}(t;\phi) = \mathbf{E}_1(t) + \mathbf{E}_2(t;\phi). \tag{10}$$

Here ϕ is the relative phase between the two field components. For $\varepsilon_1 = \varepsilon_2 = 0$ the BEOTC field (10) reduces to the OTC field while for $\varepsilon_1 = \varepsilon_2 = 1$ it becomes the bicircular field (the relative phase of our current BEOTC field should be set to $\phi = \pi/2$ to obtain the bicircular field used in ref. 32). Examples of BEOTC fields are exhibited in ref. 34. In general, the inversion symmetry $w(-\mathbf{p},\varepsilon) = w(\mathbf{p},\varepsilon)$ does not hold for the BEOTC field. The reason is that, for this symmetry to be valid, the field has to change its sign under the time translation $t \to t + T/2$.[39] Since $\mathbf{E}_1(t + T/2) = (-1)^r \mathbf{E}_1(t)$ and $\mathbf{E}_2(t + T/2;\phi) = (-1)^s \mathbf{E}_2(t;\phi) = (-1)^{s+1}\mathbf{E}_2(t;\phi+\pi)$ the inversion symmetry is only valid if r and s are odd. For r odd and s even, the inversion symmetry combined with a shift of the relative phase by π is a symmetry transformation, *i.e.*, $w(-\mathbf{p},\varepsilon,\phi+\pi) = w(\mathbf{p},\varepsilon,\phi)$. For the reflections $\hat{P}_x$ and $\hat{P}_y$ and a change of sign of the ellipticities, the symmetry of the averaged rate depends on the parity of r and s and the shift of the relative phase. This is summarized in the following relations:

$$\bar{w}(p_x,p_y,\varepsilon_1,\varepsilon_2,\phi) = \begin{cases} \bar{w}(p_x,-p_y,-\varepsilon_1,-\varepsilon_2,\phi+\pi) \text{ for } s \text{ even or odd,} \\ \bar{w}(-p_x,p_y,-\varepsilon_1,-\varepsilon_2,\phi) \text{ for } s \text{ even,} \\ \bar{w}(-p_x,p_y,-\varepsilon_1,-\varepsilon_2,\phi+\pi) \text{ for } s \text{ odd,} \end{cases} \tag{11}$$

which is valid for r odd.

3 Numerical results

3.1 Elliptical field

We first consider ionization of Ar atoms by a monochromatic elliptically polarized laser field with the intensity $I = E_1{}^2 = 2 \times 10^{14}$ W cm^{-2} and the frequency $\omega_1 = \omega$ corresponding to the fundamental wavelength of 1300 nm. In Fig. 1 we present the differential ionization rate for emission in the direction of the semi-major axis of the polarization ellipse ($\theta = 0°$) for various values of the ellipticity $\varepsilon_1 = \varepsilon$, as indicated in the panel, calculated from eqn (2) incorporating both the direct and the rescattered electrons. The plateau of the rescattered electrons is

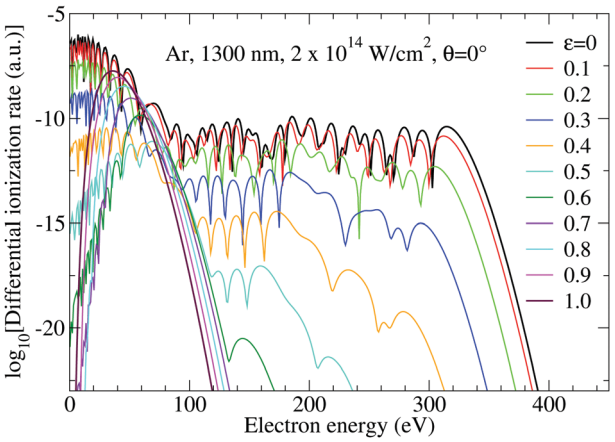

Fig. 1 The logarithm of the differential ionization rate of Ar atoms as a function of the photoelectron energy in electron volts for ionization by an elliptically polarized field for various ellipticities as indicated. Both direct and rescattered electrons are included. The laser intensity is 2 × 10^{14} W cm^{-2}, the wavelength is 1300 nm, and emission is in the direction of the semi-major axis of the polarization ellipse.

longest for linear polarization ($\varepsilon = 0$; the plateau extends up to $10U_p$, *i.e.* up to 316 eV), while it is completely absent for circular polarization ($\varepsilon = 1$). With increasing ellipticity both the plateau height and its length quickly decrease and a multiplateau structure in the spectrum of the rescattered electrons appears. This is explained using quantum-orbit theory in ref. 41 and 42. The spectrum of the direct electrons extends up to about $2U_p = 63$ eV.

Fig. 2 exhibits the corresponding photoelectron momentum distributions for various ellipticities, evaluated again from eqn (2). For linear polarization (upper left panel) the spectrum has the characteristic form of a figure eight, elongated in the direction of the major axis of the polarization ellipse (x axis).[37] For circular polarization (upper right panel) the spectrum has the form of a ring; see, *e.g.*, ref. 36. In the remaining panels we compare the photoelectron momentum distributions for positive (left panels) and negative (right panels) ellipticities. We see that the spectrum of the direct electrons, which occupies the center of the panels and corresponds to comparatively low energies, exhibits the fourfold symmetry, while the spectrum of rescattered electrons, which is clearly visible for $\varepsilon = \pm 0.2$ and ± 0.4, only exhibits the twofold symmetry $\bar{w}(\theta) = \bar{w}(\theta + \pi)$. Opposite helicities are related by the symmetry (6), *i.e.* $\bar{w}(\theta,-\varepsilon) = \bar{w}(\pi - \theta,\varepsilon) = \bar{w}(-\theta,\varepsilon)$. For the larger values of ε, rescattering is too weak to make a difference, *cf.* Fig. 1. Hence, already for $\varepsilon = 0.6$ the fourfold symmetry of the direct electrons is essentially restored.

In Fig. 3 we display the elliptic-dichroism parameter $\delta(\mathbf{p},\varepsilon)$, eqn (7), for two values of the ellipticity. We see that $\delta(\mathbf{p},\varepsilon)$ exhibits the twofold symmetry ($\theta \leftrightarrow \theta + \pi$) and it changes its sign for $\theta \to -\theta$ and $\theta \to \pi - \theta$, which is in accordance with the relation $\delta(\mathbf{p},-\varepsilon) = -\delta(\mathbf{p},\varepsilon)$. At the center of each panel we have $\delta(\mathbf{p},\varepsilon) \approx 0$, since in this region the contribution of the direct electrons is dominant. The central region expands with increasing ε due to the increasing dominance of the direct electrons. The fact that dichroic effects become less noticeable for larger ellipticities may seem counterintuitive, but a moment of thought shows that it is due to the reduced role of rescattering. In the limit of circular polarization, there is no dichroism at all, *cf.* the upper right panel of Fig. 2.

Fig. 4 shows the angle-integrated elliptic-dichroism parameter $\Delta(E_\mathbf{p},\varepsilon)$, eqn (8), for the fixed electron energies $E_\mathbf{p} = 2U_p$, $3U_p,\ldots,9U_p$. For energies lower than $2U_p$, for which the direct electrons are dominant, $\Delta(E_\mathbf{p},\varepsilon)$ is approximately zero (not shown). For energies from $E_\mathbf{p} = 2U_p$ to $4U_p$ it is close to zero for large ellipticities, while for smaller ellipticities, for which the contribution of the rescattered electrons is noticeable, it takes on some small values. For $E_\mathbf{p} = 4U_p$, $\Delta(E_\mathbf{p},\varepsilon)$ has a minimum of -0.19 for $\varepsilon = 0.57$, while for lower energies

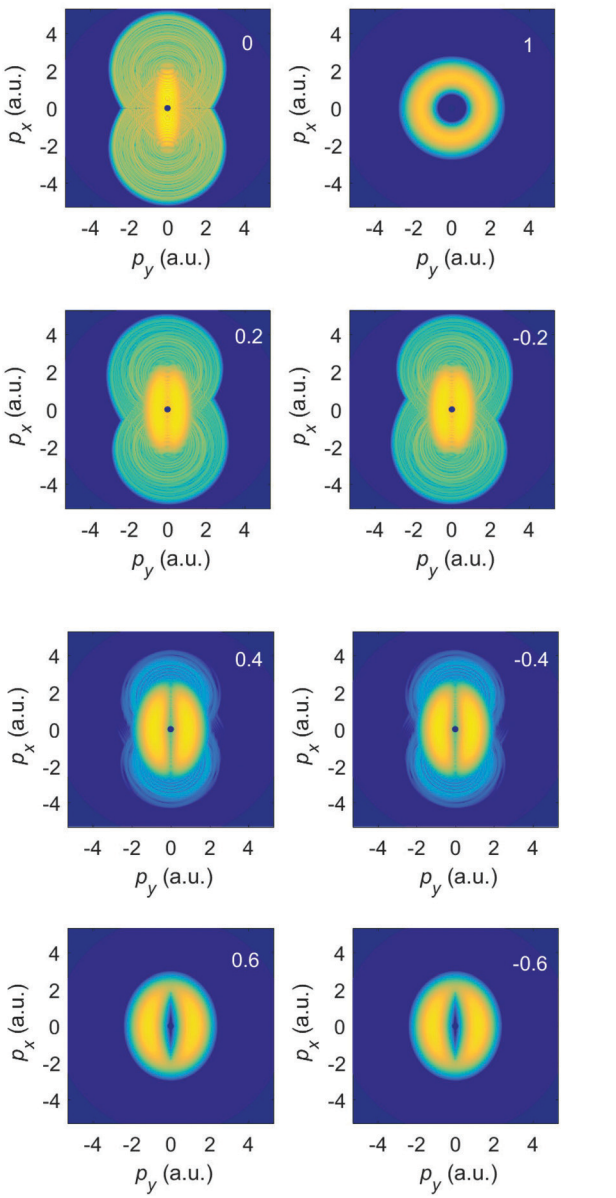

Fig. 2 The logarithm of the differential ionization rate (in a.u.) of Ar atoms, presented in false colors in the photoelectron momentum plane, for ionization by an elliptically polarized field with the ellipticity indicated in the upper right corner of each panel. Both direct and rescattered electrons are included. The false-color scale covers 13 orders of magnitude (the logarithm of the rate is between -6 to -19). The other laser parameters are as in Fig. 1.

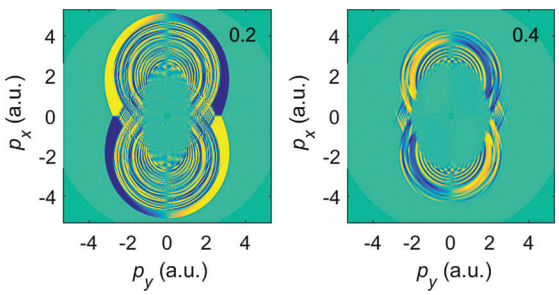

Fig. 3 The elliptic-dichroism parameter presented in false colors in the photoelectron momentum plane for ionization of Ar atoms by an elliptically polarized field with ellipticity $\varepsilon = 0.2$ (left panel) and $\varepsilon = 0.4$ (right panel), corresponding to the spectra shown in Fig. 2. The false-color scale changes from -1 (blue) to +1 (yellow). The other laser parameters are as in Fig. 1.

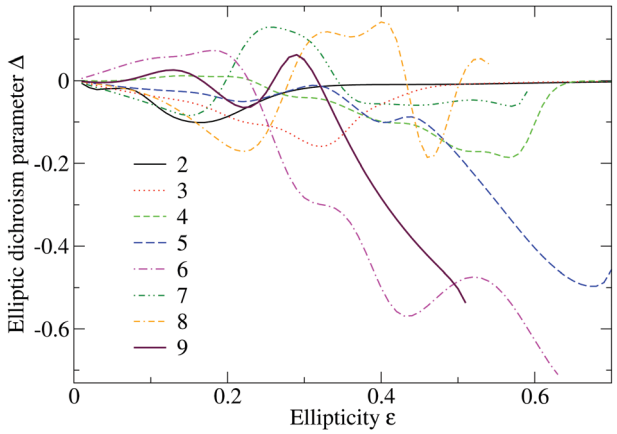

Fig. 4 Angle-integrated elliptic-dichroism parameter as a function of the ellipticity for electron energies in units of U_p as indicated. Both direct and rescattered electrons are included. The laser parameters are as in Fig. 1.

minima appear for smaller values of the ellipticity and the corresponding value of $|\Delta(E_{\mathbf{p}},\varepsilon)|$ is lower. For larger values of the energy and ellipticity the ionization rate is negligibly small and, due to loss of numerical precision owing to roundoff errors, the calculated parameter $\Delta(E_{\mathbf{p}},\varepsilon)$ is meaningless. For energies from $E_{\mathbf{p}} = 5U_p$ to $9U_p$ the parameter $|\Delta(E_{\mathbf{p}},\varepsilon)|$ increases with increasing ellipticities and exhibits oscillations.

As we have mentioned in the introduction, for longer wavelengths the various low-energy structures become more pronounced. Therefore, we will now present results for a wavelength of 2000 nm, keeping the other parameters the same. Still, the direct electrons dominate the low-energy spectra except when the contribution of the forward-scattered electrons is enhanced by the Coulomb potential. In Fig. 5 we present the results for the differential ionization rate similarly as in Fig. 2, but now taking into account only the rescattering T-matrix element (4) and for the photoelectron energy lower than $2.2U_p$. For linear polarization, the spectrum in the top left panel has a characteristic rhombus- or diamond-like shape (compare Fig. 5 in ref. 43), while for circular polarization it has the form of a ring, similar to the upper right panel of Fig. 2. So, interestingly, for circular polarization the rescattering contribution (4) is largely proportional to the direct contribution (3). For the ellipticity $\varepsilon = \pm 0.1$ (second line) the diamond-like structure has become slightly tilted and deformed, in opposite directions for opposite helicity, and the rate satisfies the symmetries for the rescattered electrons explained above. However, for the central part of the spectrum, for $p_y = 0$ and $|p_x| < 1$ the rescattered-electron-induced difference between the spectra for $\varepsilon = 0.1$ and $\varepsilon = -0.1$ is hardly visible. This part contains the LES, which for linear polarization is located at $|p_x| \approx 0.75$ a.u. For $\varepsilon = \pm 0.1$, a cross-like pattern in the middle of the plot appears to augment the LES; interestingly, the vertical arm does not tilt with the ellipticity while the horizontal does. For the ellipticity $\varepsilon = \pm 0.2$ a new structure has appeared: two elongated vertical kidney-shaped distributions parallel to the major polarization axis at about $p_y = \pm 0.75$ a.u., which

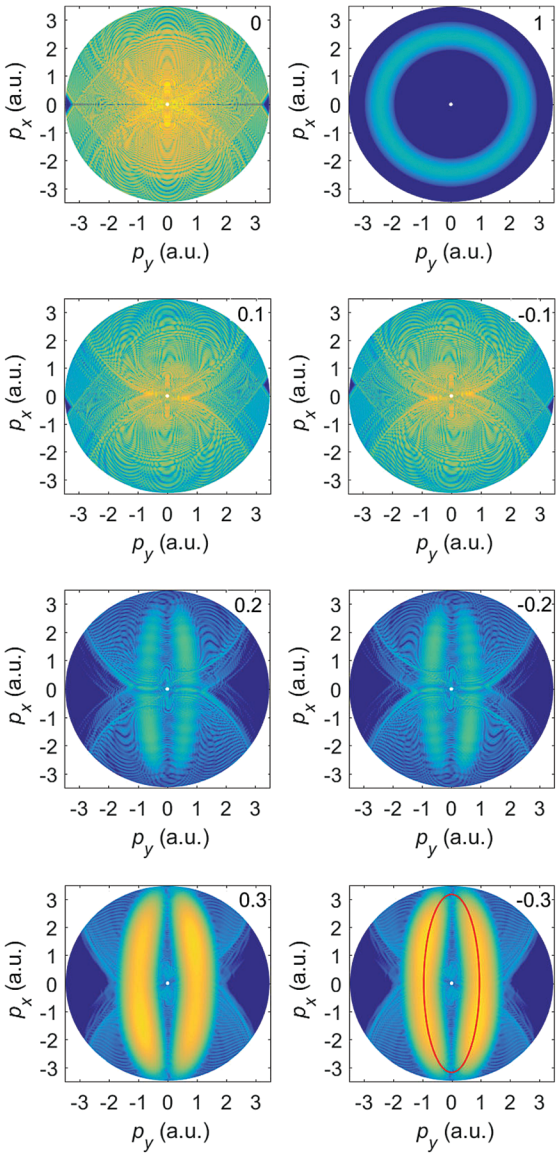

Fig. 5 The logarithm of the differential ionization rate (in a.u.) of Ar atoms for the rescattered electrons, presented in false colors in the photoelectron momentum plane, for ionization by an elliptically polarized field with wavelength 2000 nm and intensity 2×10^{14} W cm^{-2}, with the ellipticities given in the upper right corner of each panel. The false-color scale covers 6 orders of magnitude (the logarithm of the rate is between −9 and −15), except for the bottom panels for which it covers 8 orders of magnitude (the logarithm of the rate is between −11 and −19). In the bottom right panel the vector potential of the laser field is depicted by a red line.

together look like the two halves of a coffee bean. For larger ellipticities this structure persists and becomes even more pronounced. Its shape approaches the total distribution (direct plus rescattered), which for the shorter wavelenght of 1300 nm is shown in Fig. 2, in the same way as the rescattering contribution for circular polarization approaches the total contribution (upper right panels of Fig. 2 and 5).

Momentum distributions of the direct electrons only are analyzed in ref. 44 and 45. With increasing ellipticity the *shapes*

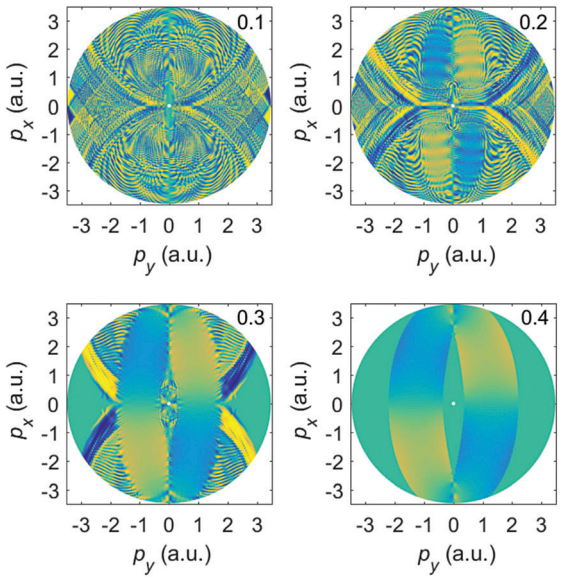

Fig. 6 The elliptic-dichroism parameter presented in false colors in the photoelectron momentum plane for ionization of Ar atoms by an elliptically polarized field with the ellipticities denoted in the upper right corner of each panel. The false-color scale changes from −1 (blue) to +1 (yellow). The other laser parameters are as in Fig. 5, which is based on the rescattered electrons only.

of the rescattering momentum distributions appear to become closer to those of the direct electrons. However, the *yields* are not the same. This becomes evident by inspection of the elliptic-dichroism parameter, which we present in Fig. 6 for ellipticities from 0.1 to 0.4. For $\varepsilon > 0.2$, the kidney structures appear and immediately dominate the momentum distribution. However, the elliptic-dichroism parameter only observes the symmetries of the rescattered electrons and not the fourfold symmetry of the direct electrons. While this is so, the complicated rescattering structures, which characterize the plot for linear ($\varepsilon = 0$) and slightly elliptical ($\varepsilon = 0.1$) polarization, have completely disappeared for $\varepsilon > 0.3$. Recalling that $\delta(\mathbf{p},\varepsilon) = 0$ for the direct electrons, we conclude that by measuring the elliptic-dichroism parameter it is possible to determine which electrons, direct or rescattered, dominate the strong-field ionization process. If the elliptic-dichroism parameter is different from zero and obeys the symmetries visible in Fig. 6, then we can say that the contribution of the shortest rescattering quantum orbit is dominant. This can be important for understanding the strong-field ionization process and explaining various experimentally observed structures.[26–28,37] We have in mind the low-energy structures on and off the polarization axis, as well as the spiderlike structures known as holograms, laser-induced electron diffraction which can be used for imaging ultrafast molecular dynamics, *etc*. It would be interesting to see how these structures change with introducing laser ellipticity and how they will manifest themselves in the momentum distributions of elliptic dichroism.

Comparing the spectra calculated above and the corresponding results for the elliptical dichroism on the one hand with experimental data on the other is difficult due to the effect of the Coulomb potential, which in our work is not fully incorporated beyond the wave functions of the initial bound state and the description of rescattering in the first-order Born approximation. It is well known since the early days of ATI that experimentally measured spectra for ionization of rare-gas atoms by elliptically polarized fields violate the fourfold symmetry predicted by the strong-field approximation for the direct electrons and only preserve the twofold inversion symmetry.[15] This reduction from fourfold to twofold symmetry is reproduced by theory once the action of the Coulomb potential is taken into account.[46–48] The coffee-bean like structures, which are so obvious in Fig. 2 and 6, are also well known except that both in experiments and in simulations that incorporate the Coulomb potential (such as CTMC (classical-trajectory Monte Carlo) simulations[49–52]) the two halves of the coffee bean are shifted *versus* one another along the major polarization axis, owing to the action of the Coulomb potential on the liberated electron. (We mention in passing that for the shorter wavelength of 400 nm the coffee-bean structure is not yet visible and the spectrum is completely dominated by the ATI rings[52]). The two halves of the coffee bean start shifting at or just below $\varepsilon = 0.2$ (see Fig. 2 and 6), in agreement with ref. 53, which presents both CTMC theory and experiments on rare gases.

At the same ellipticity of about $\varepsilon = 0.2$, the population along the major polarization axis starts thinning out (notice, especially, Fig. 2 for $|\varepsilon| = 0.4$). For $|\varepsilon| \geq 0.6$, the spectrum begins to approach the characteristics of circular polarization with its rotational symmetry, and the population along the major axis rises again.[44] We remark in passing that the staircase structure of the spectrum observed and discussed in ref. 41 and 42 (*cf.* also Fig. 1) only develops along the major axis. In general, the electron population is concentrated about the curve $\mathbf{p} = -\mathbf{A}(t)$ as predicted by the simple-man model. The maxima of the momentum distribution correspond to those times t where the electric field $|\mathbf{E}(t)|$ is maximal, that is, where the modulus of the vector potential is minimal,[44] *i.e.*, in the direction of the minor polarization axis. For $\varepsilon = -0.3$, the curve $\mathbf{A}(t)$ is displayed in the lower right panel of Fig. 5.

3.2 BEOTC field

In this subsection we analyze the photoelectron spectra for ionization of Ar atoms by ω–2ω ($r = 1$ and $s = 2$) and ω–3ω ($r = 1$ and $s = 3$) BEOTC fields having the fundamental wavelength 1300 nm. For simplicity we suppose that the component ellipticities and intensities are equal, *i.e.*, that $\varepsilon_1 = \varepsilon_2 = \varepsilon$ and $I_1 = {E_1}^2 = I_2 = {E_2}^2 = 1 \times 10^{14}$ W cm^{-2}. The relative phase is fixed to $\phi = 0$ or to $\phi = \pi$.

In Fig. 7 we present the differential ionization rate for the ω–2ω BEOTC field for the ellipticities $\varepsilon = 0$, 0.2, 0.4, 0.6, 0.8, 1.0, for the electron emission angle $\theta = 90^\circ$, and for the relative phase $\phi = 0$ (upper panel) and $\phi = \pi$ (lower panel), calculated from eqn (2) with both direct and rescattered electrons included. In all cases presented the rescattering plateau is clearly visible. For the OTC field ($\varepsilon = 0$) and for $\phi = 0$ the plateau exhibits pronounced fast oscillations and the cutoff is

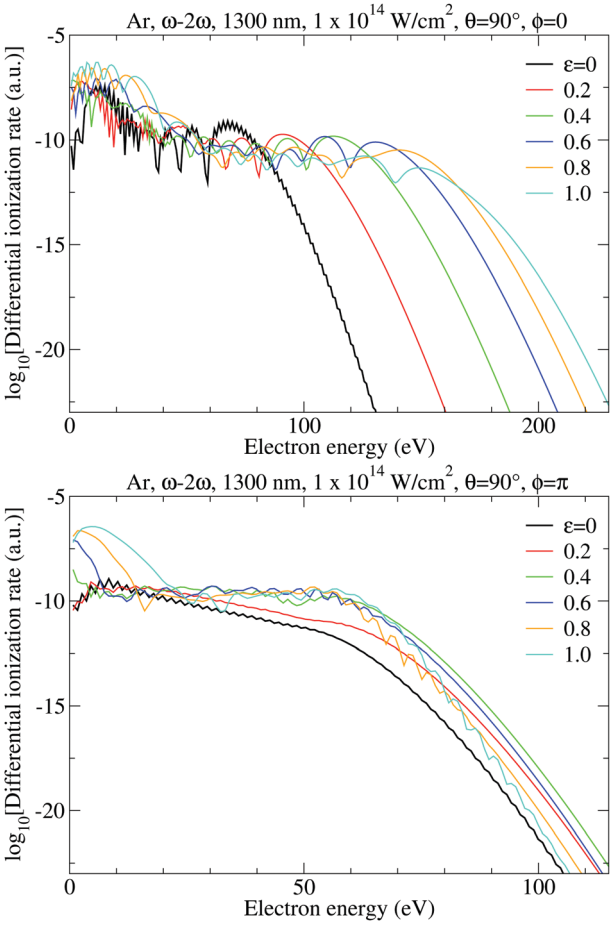

Fig. 7 The logarithm of the differential ionization rate of Ar atoms as a function of the photoelectron energy in electron volts for ionization by an ω–2ω BEOTC field with the ellipticities $\varepsilon = \varepsilon_1 = \varepsilon_2$ denoted in the panels. Both the direct and the rescattered electrons are included. The intensities of the field components are $I_1 = I_2 = 1 \times 10^{14}$ W cm^{-2}, the fundamental wavelength is 1300 nm, and emission is in the direction of the semi-minor axis of the polarization ellipse (y axis). The relative phase is $\phi = 0$ (upper panel) and $\phi = \pi$ (lower panel).

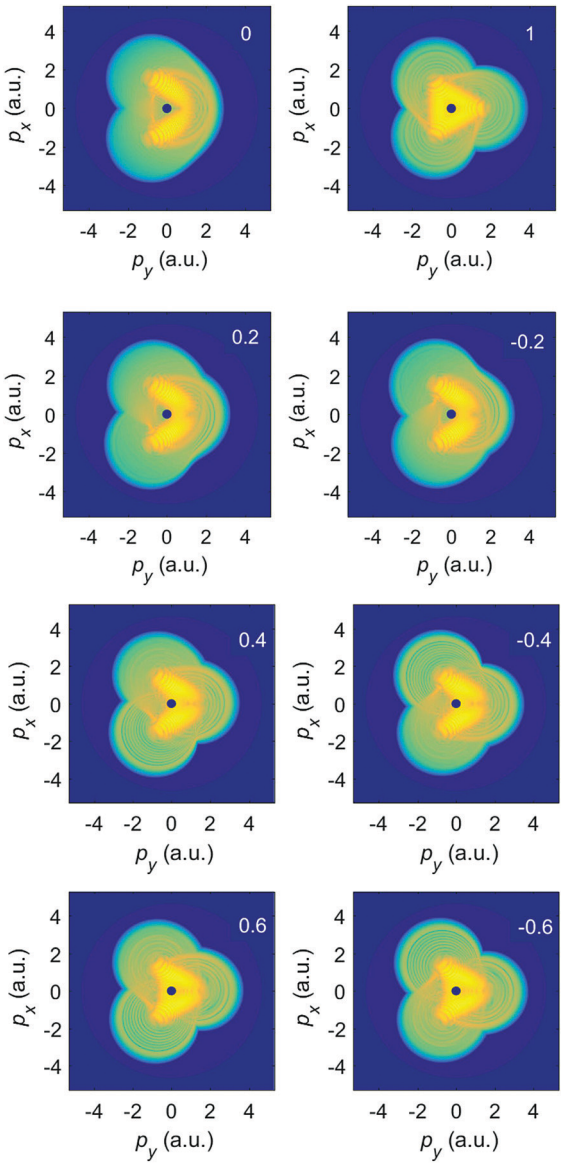

Fig. 8 The logarithm of the differential ionization rate (in a.u.) of Ar atoms, presented in false colors in the photoelectron momentum plane, for ionization by an ω–2ω BEOTC field with the ellipticity $\varepsilon = \varepsilon_1 = \varepsilon_2$ denoted in the upper right corner of each panel, and with the relative phase $\phi = 0$. Both the direct and the rescattered electrons are included. The false-color scale covers 13 orders of magnitude (the logarithm of the rate extends from −6 down to −19). The other laser parameters are as in Fig. 7.

at 80 eV, while for $\phi = \pi$ the plateau is more inclined and without fast oscillations, while the cutoff is at 60 eV. For larger ellipticities the plateau is almost two times longer for the relative phase $\phi = 0$ than for $\phi = \pi$. Clearly, the relative phase ϕ can serve as a powerful control parameter.

More information about the ionization process is contained in the photoelectron momentum distributions, presented in Fig. 8 for the relative phase $\phi = 0$ and for various ellipticities, similarly to the case of the elliptically polarized monochromatic field in Fig. 2. The top left and right panels correspond, respectively, to the two limiting cases of the OTC field ($\varepsilon = 0$) and the bicircular field ($\varepsilon = 1$) and their momentum distributions agree with previous results.[32,54] From the remaining panels we see that the rotational and reflection symmetries, which are characteristic for the OTC and bicircular fields, are violated for our more general BEOTC field. Comparing the left and right panels confirms that the simultaneous reversal of the sign of p_x and the sign of the ellipticity is a symmetry transformation. This is in accordance with the rule (11) (the $s = 2$ case in the second line).

Numerical results for the same BEOTC field parameters as in Fig. 8, but with only the direct electrons included are shown in Fig. 9, for the ellipticities denoted in the upper right corner of each panel. We see that the momentum distributions are concentrated about the momenta on a parametric plot of $\mathbf{p} = -\mathbf{A}(t_0)$, which is depicted by a red curve in each panel. This is as predicted by the simple-man model. The curve is also an approximate solution of the saddle-point equation for the

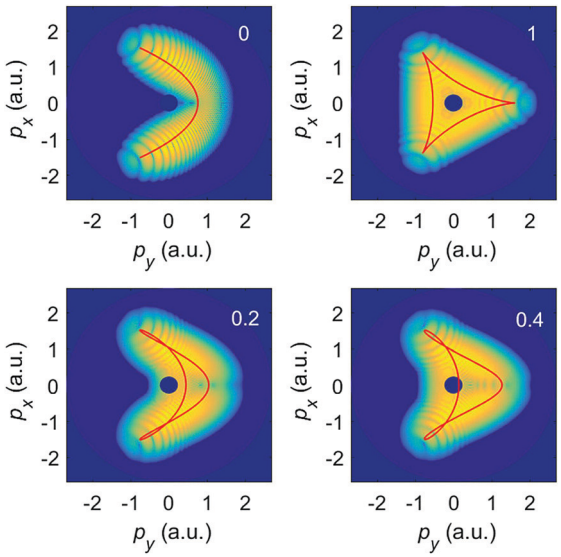

Fig. 9 The logarithm of the differential ionization rate (in a.u.) of Ar atoms, presented in false colors in the photoelectron momentum plane, for ionization by the same BEOTC field as in Fig. 8, but with only the direct electrons included. The false-color scale covers 6 orders of magnitude (the logarithm of the rate extends from −6 down to −12). The red curves depict the negative vector potential $-\mathbf{A}(t_0)$ for ellipticities as denoted in the upper right corner of each panel.

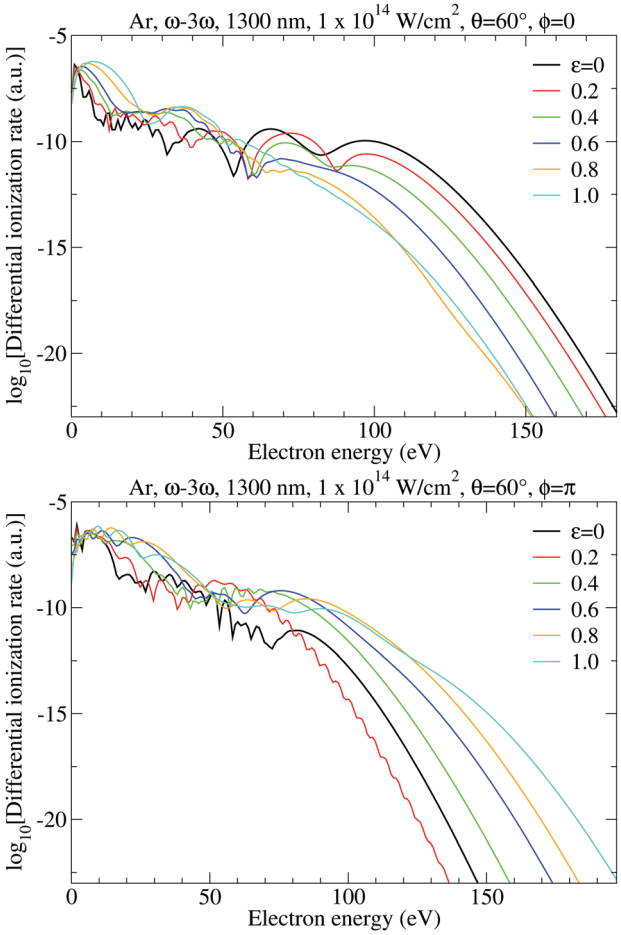

Fig. 10 The logarithm of the differential ionization rate of Ar atoms as a function of the photoelectron energy in electron volts for ionization by an ω–3ω BEOTC field with the ellipticities $\varepsilon = \varepsilon_1 = \varepsilon_2$ as indicated. Both the direct and the rescattered electrons are included. The intensities of the field components are $I_1 = I_2 = 1 \times 10^{14}$ W cm^{-2}, the fundamental wavelength is 1300 nm, and the emission is in the direction $\theta = 60°$. The relative phase is $\phi = 0$ (upper panel) and $\phi = \pi$ (lower panel).

direct electrons (in the saddle-point approximation the integral over the ionization time in eqn (3) can be approximated by a sum over the saddle-point solutions t_{0s} of the equation $[\mathbf{p} + \mathbf{A}(t_{0s})]^2 = -2I_p$[36,45]). The momentum distributions in Fig. 9 satisfy the same reflection symmetries as the parametric plots, regardless of the time evolution of each curve (clockwise or counterclockwise). These symmetries are broken once rescattering is taken into account, as is clear by comparison with Fig. 8.

Fig. 10 displays the differential ionization rate similarly to Fig. 7 but for the ω–3ω BEOTC field and for the emission angle $\theta = 60°$. For the relative phase $\phi = 0$ the plateau length decreases with increasing ellipticities, while for $\phi = \pi$ the plateau is longer for higher ellipticities.

For an ω–3ω BEOTC field the spectra in Fig. 11 satisfy inversion symmetry, *i.e.*, the photoelectron momentum distribution is invariant with respect to the transformation $\mathbf{p} \to -\mathbf{p}$. However, they are not invariant with respect to the simultaneous change of the sign of the ellipticity and one of the momentum components, as was the case in Fig. 8. To obtain symmetry, it is also necessary to change the relative phase by π (see Fig. 13).

Comparing the left panels of Fig. 12 with the right panels of Fig. 8 shows that the momentum distributions for the ω–2ω BEOTC field are invariant with respect to the simultaneous transformations $\varepsilon \leftrightarrow -\varepsilon$, $p_y \leftrightarrow -p_y$, and $\phi \leftrightarrow \phi + \pi$, in agreement with the rule (11). On the other hand, comparing the left panels of Fig. 13 with the right panels of Fig. 11 we conclude that for the ω–3ω BEOTC field, in addition to the inversion symmetry, two symmetry transformations are valid: (i) $\varepsilon \leftrightarrow -\varepsilon$, $\phi \leftrightarrow \phi + \pi$, $p_x \leftrightarrow -p_x$ and (ii) $\varepsilon \leftrightarrow -\varepsilon$, $\phi \leftrightarrow \phi + \pi$, $p_y \leftrightarrow -p_y$. This is again in accordance with the rule (11).

In Fig. 14 we show the elliptic-dichroism parameter $\delta(\mathbf{p},\varepsilon)$, eqn (7), for two values of the ellipticity. We see that $\delta(\mathbf{p},\varepsilon)$ changes its sign for $p_x \to -p_x$, *i.e.*, $\theta \to \pi - \theta$, as required by eqn (11) and the relation $\delta(\mathbf{p},-\varepsilon) = -\delta(\mathbf{p},\varepsilon)$. In addition, we see that the symmetry transformation $\varepsilon \leftrightarrow -\varepsilon$, $\phi \leftrightarrow \phi + \pi$, $p_y \leftrightarrow -p_y$, is also satisfied.

Fig. 15 displays the elliptic dichroism parameter for the ω–3ω BEOTC field. Now the inversion symmetry $\mathbf{p} \to -\mathbf{p}$ is satisfied for all phases and ellipticities. In addition, the above-mentioned symmetries (i) and (ii) are also satisfied. Especially for the higher ellipticity $\varepsilon = 0.4$, the plots identify regions of very high contrast wherein ionization into a final state with certain momenta (p_x,p_y) is much more likely by a field with one value of the helicity rather than its opposite. There are also extended regions, especially near the center of the plot, where the rate of ionization is practically independent of the helicity indicating

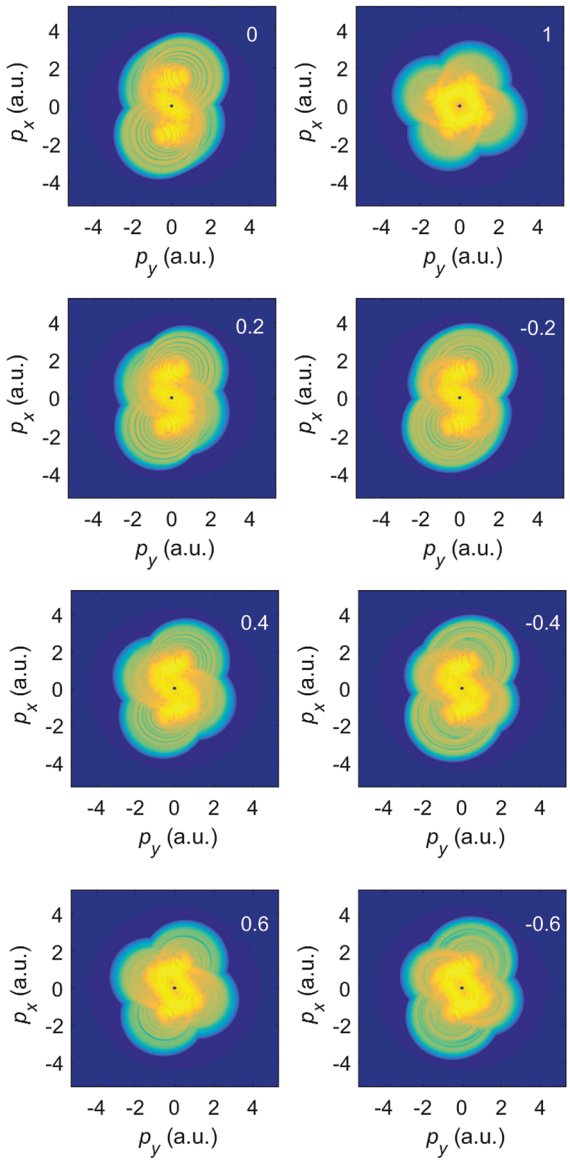

Fig. 11 The logarithm of the differential ionization rate (in a.u.) of Ar atoms, presented in false colors in the photoelectron momentum plane, for ionization by an ω–3ω BEOTC field with the ellipticity $\varepsilon = \varepsilon_1 = \varepsilon_2$ denoted in the upper right corner of each panel, and with the relative phase $\phi = 0$. Both the direct and the rescattered electrons are included. The false-color scale covers 13 orders of magnitude (the logarithm of the rate is between −6 and −19). The other laser parameters are as in Fig. 10.

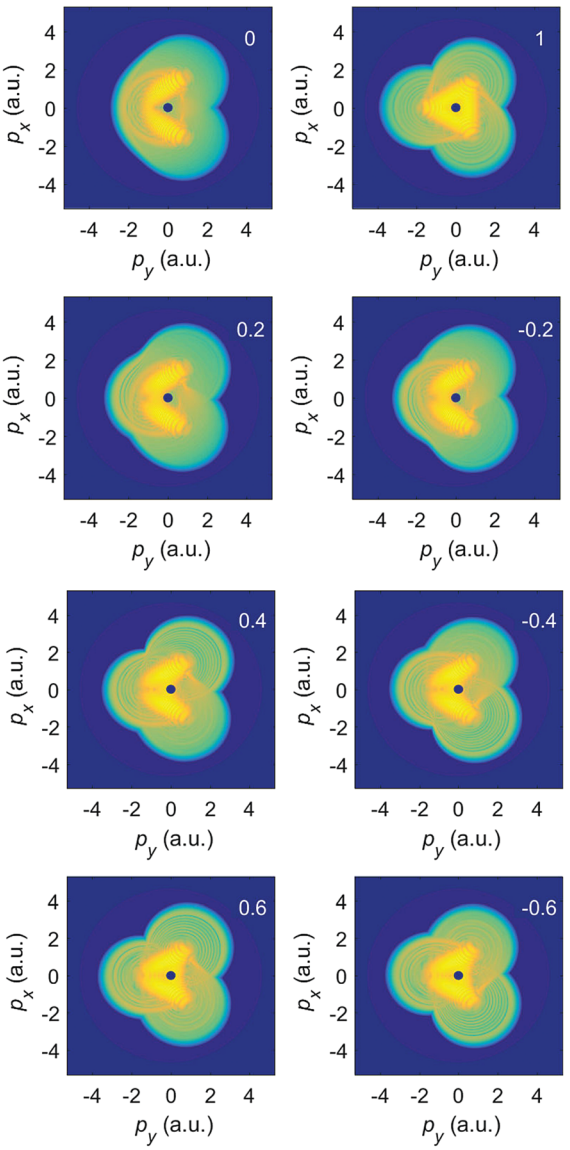

Fig. 12 Same as Fig. 11, but for the ω–2ω BEOTC field with the relative phase $\phi = \pi$.

that rescattering plays hardly any role for these final-state momenta.

Finally, we will focus on comparatively low momenta and the transition from the pure OTC field ($\varepsilon = 0$) towards the bicircular field ($\varepsilon = 1$). Fig. 16 exhibits enlargements of the panels of Fig. 8 with positive ellipticity, with only rescattered electrons included, and with a color scale that is more adapted to the analysis of the central region. The ponderomotive potential of the ω field component is 0.58 a.u.; for linear polarization the first LES corresponds to the momentum $p_{\mathrm{LES}} \approx \sqrt{2 \times 0.1 U_p} = 0.34$ a.u., which should set the stage also for the LESs due to the OTC or BEOTC fields. For $\varepsilon = 0$, this region is rather thinly populated. The structures that are visible observe the $p_x \rightarrow -p_x$ symmetry of the OTC field. With increasing ε various much more pronounced structures develop. They are all characterized by a strong violation of the afore-mentioned symmetry. For larger momenta, some spiral arms start to develop as they are characteristic of the bicircular field where their directionality is related to the relative helicity of the bicircular field.[18,32] However, in the present case the arms protrude in either direction. For further increasing ellipticity, the spectra approach those of the bicircular field and the pertinent rotational symmetry. Interestingly, this happens more quickly in the outer momentum regions.

The bottom panel of Fig. 16 exhibits the elliptic-dichroism parameter for $\varepsilon = 0.4$ and $\varepsilon = 0.6$. We can see that $\delta(\mathbf{p},\varepsilon)$ is large

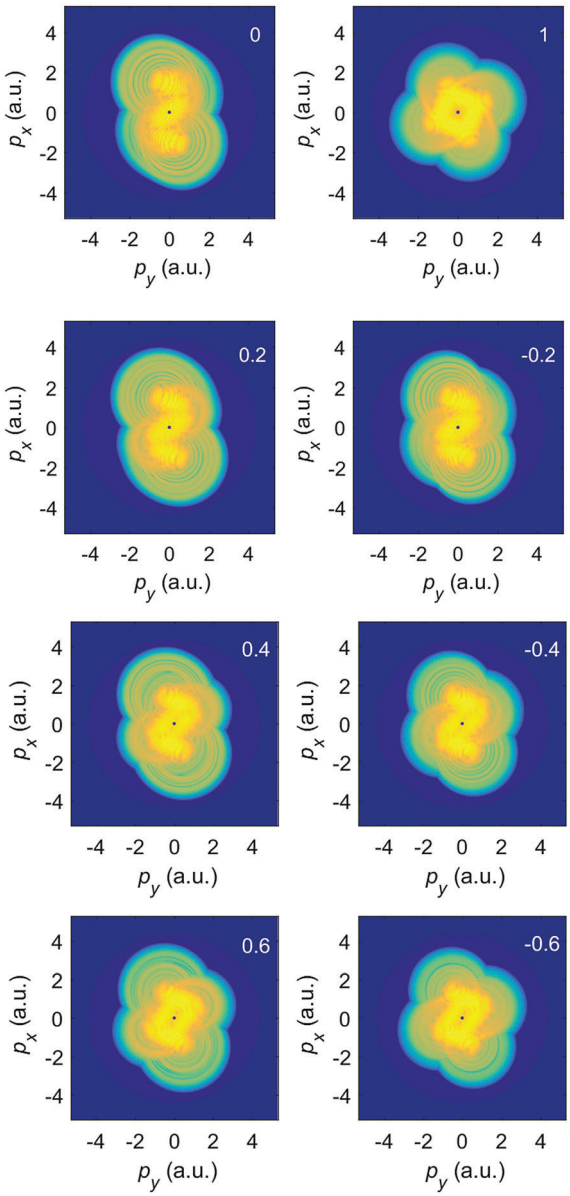

Fig. 13 The logarithm of the differential ionization rate (in a.u.) of Ar atoms, presented in false colors in the photoelectron momentum plane, for ionization by an ω–3ω BEOTC field with the ellipticity $\varepsilon = \varepsilon_1 = \varepsilon_2$ denoted in the upper right corner of each panel, and with the relative phase $\phi = \pi$. The false-color scale covers 13 orders of magnitude (the logarithm of the rate is between −6 and −19). The other laser parameters are as in Fig. 10.

in an extended region of the spectrum about $(p_x,p_y) = (-1,-1)$ a.u. The upper right panel of Fig. 14 presents the spectrum due to both the direct and the rescattered electrons. This plot shows a large region with momenta $|p_x| \leq 1$ and $|p_y| \leq 2$ where $\delta(\mathbf{p},\varepsilon) \approx 0$. This reveals that overall rescattering contributes little to this region, even though taken by itself its helicity asymmetry is strong. We conclude that by measuring the momentum distribution of the elliptic-dichroism parameter one can obtain information about the significance of rescattering, *i.e.*, information about the rescattering target.

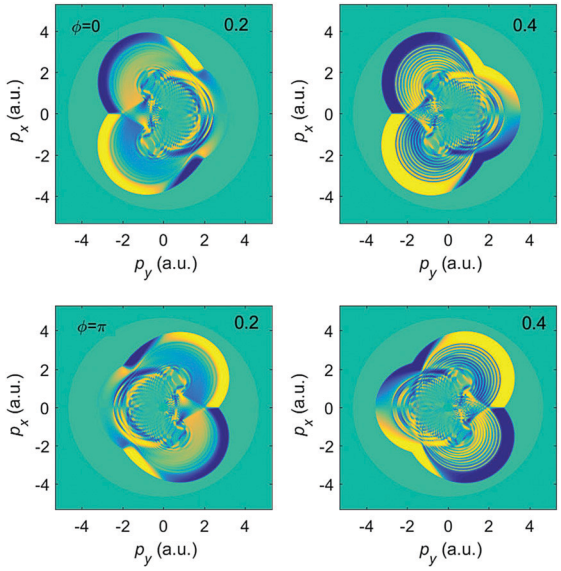

Fig. 14 The elliptic-dichroism parameter $\delta(\mathbf{p},\varepsilon)$ presented in false colors in the photoelectron momentum plane for ionization of Ar atoms by an ω–2ω BEOTC field with ellipticity $\varepsilon = 0.2$ (left panels) and $\varepsilon = 0.4$ (right panels) and relative phase $\phi = 0$ (upper panels) and $\phi = \pi$ (lower panels) corresponding to the spectra of Fig. 8 ($\phi = 0$) and Fig. 12 ($\phi = \pi$). The false-color scale changes from −1 (blue) to +1 (yellow). The other laser parameters are as in Fig. 7.

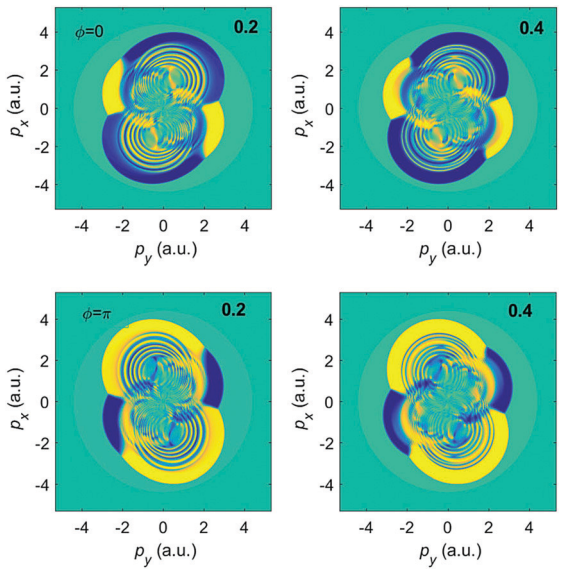

Fig. 15 The elliptic-dichroism parameter presented in false colors in the photoelectron momentum plane for ionization of Ar atoms by an ω–3ω BEOTC field with ellipticity $\varepsilon = 0.2$ (left panels) and $\varepsilon = 0.4$ (right panels) and relative phase $\phi = 0$ (upper panels) and $\phi = \pi$ (lower panels), corresponding to the spectra of Fig. 11 ($\phi = 0$) and Fig. 13 ($\phi = \pi$). The false-color scale changes from −1 (blue) to +1 (yellow). The other laser parameters are as in Fig. 10.

4 Conclusions

Low-energy photoelectrons liberated in strong-field ionization of atoms are mostly generated as direct electrons, *i.e.* electrons

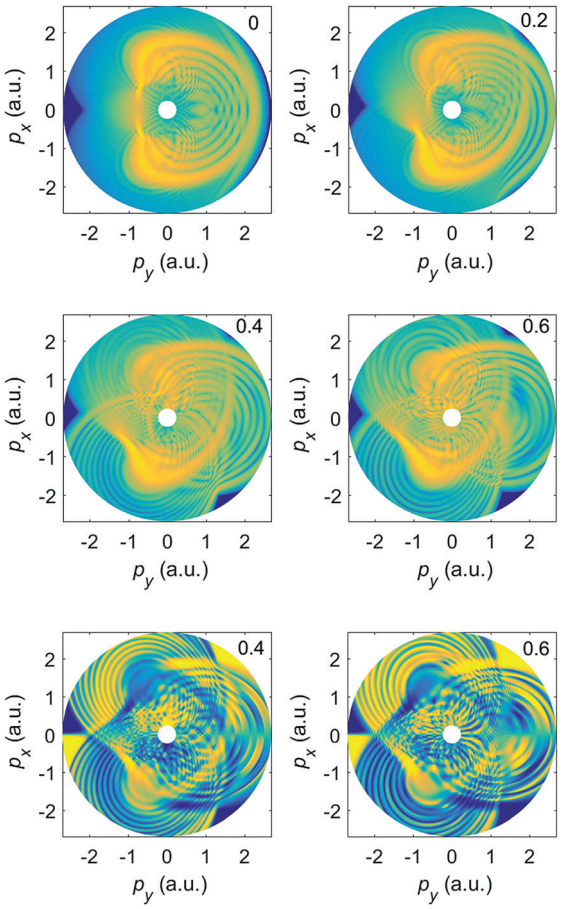

Fig. 16 Enlargement of the central parts of Fig. 8 for the same parameters but positive ellipticities only and with only the rescattered electrons included. The color scale includes five orders of magnitude. The bottom panel shows the corresponding elliptic-dichroism parameter for the ellipticities ε = 0.4 and ε = 0.6.

that directly go to the detector after ionization. On the other hand, electrons reach high energies as a consequence of rescattering off their parent ion. Due to their different ionization mechanism the photoelectron momentum distributions display different characteristics for direct and rescattered electrons. For ionization by an elliptical field, in addition to the twofold inversion symmetry $\bar{w}(-\mathbf{p}) = \bar{w}(\mathbf{p})$, which is obeyed by all electrons, the direct-electron spectra satisfy the fourfold symmetry $\bar{w}^{\mathrm{dir}}(\theta) = \bar{w}^{\mathrm{dir}}(\pi - \theta) = \bar{w}^{\mathrm{dir}}(-\theta)$ and they do not depend on the sign of the ellipticity, *i.e.* $\bar{w}^{\mathrm{dir}}(\mathbf{p},\varepsilon) = \bar{w}^{\mathrm{dir}}(\mathbf{p},-\varepsilon)$. Therefore, the elliptic-dichroism parameter is equal to zero for the direct electrons. This symmetry is not valid for the rescattered electrons since for these electrons the time-inversion symmetry is violated: the time ordering—first ionization and then rescattering—is crucial. However, instead of this symmetry, the photoelectron spectra for elliptical polarization satisfy the symmetry $\bar{w}(\pi - \theta,-\varepsilon) = \bar{w}(-\theta,-\varepsilon) = \bar{w}(\theta,\varepsilon)$. The resulting symmetries of the elliptic-dichroism parameter are analyzed in detail in the first part of the paper. An important discovery is that for ellipticities higher than $|\varepsilon|$ = 0.2 the electron momentum distribution forms a structure parallel to the major polarization axis that is reminiscent of a coffee bean. For further increasing ellipticity, the momentum dependence of the elliptic-dichroism parameter simplifies more and more, indicating that fewer and fewer quantum orbits contribute. A quantum-orbit analysis of the low-energy structures for elliptical polarization has not been carried out yet. Analyzing the symmetry properties of the measured momentum distribution of the elliptic-dichroism parameter the mechanism of strong-field ionization can be identified. If rescattering is the dominant mechanism we can use the elliptic-dichroism distributions to obtain information about the atomic and molecular structure and dynamics. For example, one can explore the evolution of a molecular shape resonance along a chemical bond as it is stretching, as has been done for a linearly polarized field in ref. 55. Or one can trace the subfemtosecond molecular dynamics as was done in ref. 56 for an elliptically polarized laser field.

We also considered the BEOTC field for which the above-mentioned symmetries are, in general, violated. Rather, we have identified particular symmetries that depend on the parity of r and s for the $r\omega$–$s\omega$ BEOTC field that we used and on the relative phase between the field components. These symmetries are summarized in relation (11) and the preceding text. All the afore-mentioned symmetries of the photoelectron momentum distributions and the elliptic-dichroism parameter are illustrated by plots obtained using calculations based on the (improved) strong-field approximation.

We restricted ourselves to equal ellipticities and intensities for the two BEOTC components. In general, exploiting the possibilities of this parameter space, certainly the appearance of dichroic effects can be greatly expanded. An example is the investigation of the effect of the intensity ratio[57] and the ellipticities[58] of the bicircular field components on high-order harmonic generation. The analysis described above of the elliptic-dichroism parameter in atomic (H)ATI by the BEOTC field, and, in general, in tailored fields, can be generalized to molecular systems. For this we can use our molecular improved strong-field approximation (see ref. 59 and references therein). In the future we will investigate how elliptic dichroism depends on molecular parameters such as the internuclear distance and the molecular orientation. The molecular structure and its symmetry are imprinted in the interference minima that are observed in the photoelectron momentum distributions in HATI by a linearly polarized laser field. This was predicted in ref. 59 and observed in ref. 60 and 61. We expect that such interferences in tailored fields will be particularly noticeable in the momentum distribution of the elliptic-dichroism parameter, analogous to that presented in Fig. 14 and 15 for the argon atom. As another example, the position within a molecule where the electron is photoemitted can be resolved, see the recent work[62] in which an OTC field was applied. Extension to a BEOTC field and study of the elliptic dichroism will yield additional transverse information.

Author contributions

All authors contributed equally to the paper.

Conflicts of interest

There are no conflicts to declare.

Acknowledgements

We acknowledge support by the Ministry of Science, Higher Education and Youth, Canton Sarajevo, Bosnia and Herzegovina, and the Alexander von Humboldt Foundation.

References

1 I. Powis, *Adv. Chem. Phys.*, 2008, **138**, 267.
2 B. Ritchie, *Phys. Rev. A*, 1976, **13**, 1411.
3 N. Böwering, T. Lischke, B. Schmidtke, N. Müller, T. Khalil and U. Heinzmann, *Phys. Rev. Lett.*, 2001, **86**, 1187.
4 L. Nahon, G. A. Garcia, C. J. Harding, E. Mikajlo and I. Powis, *J. Chem. Phys.*, 2006, **125**, 114309.
5 C. Lux, M. Wollenhaupt, T. Bolze, Q. Liang, J. Kohler, C. Sarpe and T. Baumert, *Angew. Chem., Int. Ed.*, 2012, **51**, 5001.
6 C. S. Lehmann, N. B. Ram, I. Powis and M. H. M. Janssen, *J. Chem. Phys.*, 2013, **139**, 234307.
7 C. Lux, A. Senftleben, C. Sarpe, M. Wollenhaupt and T. Baumert, *J. Phys. B*, 2016, **49**, 02LT01.
8 S. Beaulieu, A. Ferré, R. Géneaux, R. Canonge, D. Descamps, B. Fabre, N. Fedorov, F. Légaré, S. Petit, T. Ruchon, V. Blanchet, Y. Mairesse and B. Pons, *New J. Phys.*, 2016, **18**, 102002.
9 K. Fehre, S. Eckart, M. Kunitski, C. Janke, D. Trabert, J. Rist, M. Weller, A. Hartung, M. Pitzer, L. P. H. Schmidt, T. Jahnke, R. Dörner and M. S. Schöffler, *Phys. Rev. Res.*, 2019, **1**, 033045.
10 K. Fehre, S. Eckart, M. Kunitski, C. Janke, D. Trabert, M. Hofmann, J. Rist, M. Weller, A. Hartung, L. P. H. Schmidt, T. Jahnke, H. Braun, T. Baumert, J. Stohner, P. V. Demekhin, M. S. Schöffler and R. Dörner, *Phys. Rev. Lett.*, 2021, **126**, 083201.
11 K. Fehre, *et al.*, *Phys. Rev. Lett.*, 2021, **127**, 103201.
12 C. S. Lehmann and K. Weitzel, *Phys. Chem. Chem. Phys.*, 2020, **22**, 13707.
13 A. Comby, E. Bloch, C. M. M. Bond, D. Descamps, J. Miles, S. Petit, S. Rozen, J. B. Greenwood, V. Blanchet and Y. Mairesse, *Nat. Commun.*, 2018, **9**, 5212.
14 P. V. Demekhin, A. N. Artemyev, A. Kastner and T. Baumert, *Phys. Rev. Lett.*, 2018, **121**, 253201.
15 M. Bashkansky, P. H. Bucksbaum and D. W. Schumacher, *Phys. Rev. Lett.*, 1988, **60**, 2458.
16 T. Jahnke, Th Weber, A. L. Landers, A. Knapp, S. Schössler, J. Nickles, S. Kammer, O. Jagutzki, L. Schmidt and A. Czasch, *et al.*, *Phys. Rev. Lett.*, 2002, **88**, 073002.
17 J. Hofbrucker, A. V. Volotka and S. Fritzsche, *Phys. Rev. Lett.*, 2018, **121**, 053401.
18 A. Gazibegović-Busuladžić, W. Becker and D. B. Milošević, *Opt. Exp.*, 2018, **26**, 12684.
19 J. Hofbrucker, B. Böning, A. V. Volotka and S. Fritzsche, *Phys. Rev. A*, 2021, **104**, 013102.
20 A. V. Volotka, J. Hofbrucker and S. Fritzsche, *Phys. Rev. A*, 2021, **104**, L031103.
21 L. Guo, S. S. Han, X. Liu, Y. Cheng, Z. Z. Xu, J. Fan, J. Chen, S. G. Chen, W. Becker, C. I. Blaga, A. D. DiChiara, E. Sistrunk, P. Agostini and L. F. DiMauro, *Phys. Rev. Lett.*, 2013, **110**, 013001.
22 C. I. Blaga, F. Catoire, P. Colosimo, G. G. Paulus, H. G. Muller, P. Agostini and L. F. DiMauro, *Nat. Phys.*, 2009, **5**, 335.
23 W. Quan, Z. Lin, M. Wu, H. Kang, H. Liu, X. Liu, J. Chen, J. Liu, X. T. He, S. G. Chen, H. Xiong, L. Guo, H. Xu, Y. Fu, Y. Cheng and Z. Z. Xu, *Phys. Rev. Lett.*, 2009, **103**, 093001.
24 P. Agostini and L. F. DiMauro, *Adv. At., Mol., Opt. Phys.*, 2012, **61**, 117.
25 F. H. M. Faisal, *Nat. Phys.*, 2009, **5**, 319.
26 M. Möller, F. Meyer, A. M. Sayler, G. G. Paulus, M. F. Kling, B. E. Schmidt, W. Becker and D. B. Milošević, *Phys. Rev. A*, 2014, **90**, 023412.
27 Y. Huismans, *et al.*, *Science*, 2011, **331**, 61.
28 D. D. Hickstein, P. Ranitovic, S. Witte, X.-M. Tong, Y. Huismans, P. Arpin, X. Zhou, K. E. Keister, C. W. Hogle, B. Zhang, C. Ding, P. Johnsson, N. Toshima, M. J. J. Vrakking, M. M. Murnane and H. C. Kapteyn, *Phys. Rev. Lett.*, 2012, **109**, 073004.
29 W. Becker, S. P. Goreslavski, D. B. Milošević and G. G. Paulus, *J. Phys. B*, 2014, **47**, 204022.
30 D. B. Milošević, *Phys. Rev. A*, 2014, **90**, 063414.
31 M. Lein and M. Wollenhaupt, *J. Mod. Opt.*, 2018, **64**, 949.
32 D. B. Milošević and W. Becker, *Phys. Rev. A*, 2016, **93**, 063418.
33 D. Habibović, A. Gazibegović-Busuladžić, M. Busuladžić, A. Čerkić and D. B. Milošević, *Phys. Rev. A*, 2020, **102**, 023111.
34 D. B. Milošević and W. Becker, *Phys. Rev. A*, 2020, **102**, 023107.
35 D. B. Milošević, Strong-field approximation and quantum orbits, in *Computational strong-field quantum dynamics: Intense Light-Matter Interactions*, ed. D. Bauer, De Gruyter Textbook, Berlin, 2016, Chap. VII, pp. 199–221.
36 W. Becker, F. Grasbon, R. Kopold, D. B. Milošević, G. G. Paulus and H. Walther, *Adv. At., Mol., Opt. Phys.*, 2002, **48**, 35.
37 W. Becker, S. P. Goreslavski, D. B. Milošević and G. G. Paulus, *J. Phys. B*, 2018, **51**, 162002.
38 E. Hasović, M. Busuladžić, A. Gazibegović-Busuladžić, D. B. Milošević and W. Becker, *Laser Phys.*, 2007, **17**, 376.
39 W. Becker, M. Kleber, A. Lohr, G. G. Paulus, H. Walther and F. Zacher, *Laser Phys.*, 1998, **8**, 56.
40 A. Gazibegović-Busuladžić, D. B. Milošević and W. Becker, *Phys. Rev. A*, 2004, **70**, 053403.
41 R. Kopold, D. B. Milošević and W. Becker, *Phys. Rev. Lett.*, 2000, **84**, 3831.
42 P. Salières, B. Carré, L. Le Déroff, F. Grasbon, G. G. Paulus, H. Walther, R. Kopold, W. Becker, D. B. Milošević, A. Sanpera and M. Lewenstein, *Science*, 2001, **292**, 902.

43 W. Becker and D. B. Milošević, *Chin. Opt. Lett.*, 2015, **13**, 070006.
44 G. G. Paulus, F. Zacher, H. Walther, A. Lohr, W. Becker and M. Kleber, *Phys. Rev. Lett.*, 1998, **80**, 484.
45 A. Jašarević, E. Hasović, R. Kopold, W. Becker and D. B. Milošević, *J. Phys. A: Math. Theor.*, 2020, **53**, 125201.
46 S. Basile, F. Trombetta and G. Ferrante, *Phys. Rev. Lett.*, 1988, **61**, 2435.
47 S. P. Goreslavski, G. G. Paulus, S. V. Popruzhenko and N. I. Shvetsov-Shilovski, *Phys. Rev. Lett.*, 2004, **93**, 233002.
48 S. V. Popruzhenko, G. G. Paulus and D. Bauer, *Phys. Rev. A*, 2008, **77**, 053409.
49 D. Shafir, H. Soifer, C. Vozzi, A. S. Johnson, A. Hartung, Z. Dube, D. M. Villeneuve, P. B. Corkum, N. Dudovich and A. Staudte, *Phys. Rev. Lett.*, 2013, **111**, 023005.
50 M. Li, Y. Liu, H. Liu, Q. Ning, L. Fu, J. Liu, Y. Deng, C. Wu, L.-Y. Peng and Q. Gong, *Phys. Rev. Lett.*, 2013, **111**, 023006.
51 J. Yu, X. Sun, Y. Shao, M. Li, Q. Gong and Y. Liu, *Phys. Rev. A*, 2015, **92**, 043411.
52 H. Xie, M. Li, S. Luo, Y. Li, Y. Zhou, W. Cao and P. Lu, *Phys. Rev. A*, 2017, **96**, 063421.
53 M. Li, M.-M. Liu, J.-W. Geng, M. Han, X. Sun, Y. Shao, Y. Deng, C. Wu, L.-Y. Peng, Q. Gong and Y. Liu, *Phys. Rev. A*, 2017, **95**, 053425.
54 D. Habibović, W. Becker and D. B. Milošević, *Symmetry*, 2021, **13**, 1566.
55 F. Brausse, F. Bach, F. Krečinić, M. J. J. Vrakking and A. Rouzée, *Phys. Rev. Lett.*, 2020, **125**, 123001.
56 V. Hanus, S. Kangaparambil, S. Larimian, M. Dorner-Kirchner, X. Xie, M. S. Schöffler, G. G. Paulus, A. Baltuška, A. Staudte and M. Kitzler-Zeiler, *Phys. Rev. Lett.*, 2019, **123**, 263201.
57 D. B. Milošević, *Phys. Rev. A*, 2018, **98**, 033405.
58 D. B. Milošević, *J. Phys. B*, 2015, **48**, 171001.
59 M. Busuladžić, A. Gazibegović-Busuladžić, D. B. Milošević and W. Becker, *Phys. Rev. Lett.*, 2008, **100**, 203003.
60 M. Okunishi, R. Itaya, K. Shimada, G. Prümper, K. Ueda, M. Busuladžić, A. Gazibegović-Busuladžić, D. B. Milošević and W. Becker, *Phys. Rev. Lett.*, 2009, **103**, 043001.
61 R. P. Sun, X. Y. Lai, S. G. Yu, Y. L. Wang, S. P. Xu, W. Quan and X. J. Liu, *Phys. Rev. Lett.*, 2019, **122**, 193202.
62 W. Xie, J. Yan, M. Li, C. Cao, K. Guo, Y. Zhou and P. Lu, *Phys. Rev. Lett.*, 2021, **127**, 263202.